Cement and Concrete Research 42 (2012) 272–281

Contents lists available at SciVerse ScienceDirect

Cement and Concrete Research

journal homepage: http://ees.elsevier.com/CEMCON/default.asp

A numerical and experimental study of aggregate-induced shrinkage cracking in cementitious composites

Andrés Idiart [a,*], Jan Bisschop [b], Antonio Caballero [c], Pietro Lura [b,d]

[a] AMPHOS 21 Consulting, S.L., Passeig Garcia i Faria, 49-51, 08019, Barcelona, Spain, formerly at OXAND S.A., 77210, Avon, France
[b] Institute for Building Materials, ETH-Zürich, Schafmattstr. 6, 8093 Zürich, Switzerland
[c] BBR VT International, Switzerland
[d] Empa, Swiss Federal Laboratories for Materials Science and Technology, 8600 Dübendorf, Switzerland

ARTICLE INFO

Article history:
Received 20 August 2010
Accepted 28 September 2011

Keywords:
Drying (A)
Shrinkage (C)
Finite element analysis (C)
Fracture mechanics
Crack detection (B)

ABSTRACT

Aggregates in cementitious composites subject to drying lead to mechanical restraint of the matrix shrinkage, which under certain conditions may lead to internal microcracking. In the present work this phenomenon is investigated using a two-dimensional (2D) numerical model and an approximate 2D experimental approach. Experimental and simulated samples with simplified and matching spatial aggregate distributions were produced to make a quantitative comparison between experiments and model predictions. In particular, the effects of aggregate size and volume fraction on the degree of internal microcracking are assessed. The main challenges of performing a quantitative comparison are highlighted and discussed. These are related to: (i) the difficulty of designing experiments without moisture gradient effects; (ii) the experimental crack detection limit; and (iii) the role of the creep response of the matrix phase in the model. The results suggest the existence of a critical aggregate size below which aggregate-restraint does not cause detectable microcracking.

1. Introduction

Concrete subject to drying, autogenous or thermal shrinkage develops stresses when the shrinkage strains are internally or externally restrained. If the stress exceeds the tensile strength, cracks may develop. This paper focuses on quantifying internal stress and microcrack development that occurs due to the restraining effect of stiff aggregates on the shrinkage of the cement paste matrix. Aggregate-restraint is beneficial, as it reduces the shrinkage of concrete compared to plain hardened cement paste [1–3]. However, the tangential tensile stresses that develop in the shrinking matrix around aggregate particles may exceed the matrix strength and cause microcracks around aggregates [4]. Distributed microcracking may affect concrete durability as it potentially results in a loss of concrete stiffness and strength [5–7] and especially in an increase of permeability to aggressive substances such as sulfates and chlorides [8–12].

The combinations of material properties and environmental conditions under which aggregate-restraint leads to microcracking of drying concrete are not well known. Drying-induced microcracking depends on, among other factors, the stiffness of the inclusions and matrix, the creep properties and tensile strength of the cement paste, and the strength of the bond between inclusions and cement paste. A reason why the effect of these parameters is not well known is the limitation of microcrack detection techniques. Direct imaging of microcracks inside concrete using optical or scanning electron microscopy is very problematic due to sample preparation effects: (i) cutting of internally stressed concrete can easily introduce new microcracks near the cut surface [13]; (ii) shrinkage microcracks close upon rewetting during wet cutting or polishing and thus may become invisible [14,15]; (iii) dry cutting and polishing, on the other hand, will lead to the introduction of new desiccation cracks on the freshly sectioned surface [13,16]; and (iv) the random orientation of aggregate-restraint microcracks also poses a detection problem. Microcracks making a small angle (<45°) with the sample surface are generally not visible in SEM because their edges are smoothened out by polishing and they therefore do not cause a shadow effect [15]. Non-destructive techniques such as X-ray tomography lack the required resolution or contrast for a reliable quantitative (sub)microcrack detection or are limited to very small sample sizes.

The detection and analysis of aggregate-restraint (micro)cracking are facilitated in model composites containing a small number of large aggregates, either with no size grading or a simplified one. In a number of studies, plate-like specimens with large cylindrical inclusions have been used [17–21]. In such experiments, aggregate-induced desiccation cracks appear on the specimen surface and the abovementioned crack-detection problems are not relevant in that case. In bulk samples with spherical inclusions, shrinkage cracks should form an interconnected network such that they can be impregnated with a fluorescent resin before sectioning to avoid recording artificial microcracks [13,22]. The following conclusions can be drawn from the abovementioned experimental studies: radial as well as bond cracks form around the aggregate particles;

* Corresponding author. Tel.: +34 935 830 500.
E-mail address: andres.idiart@amphos21.com (A. Idiart).

0008-8846/$ – see front matter © 2011 Elsevier Ltd. All rights reserved.
doi:10.1016/j.cemconres.2011.09.013

shrinkage cracks typically occur along the shortest line connecting aggregate centers; and the amount of cracks increases with size and volume fraction of aggregates. It has also been observed that below a certain aggregate size (between 2 and 4 mm), stiff aggregates did not cause detectable radial microcracks upon drying [22,23].

In recent years, mesostructural numerical models with different levels of sophistication have been used to study the effect of aggregates on drying-induced microcracking [24–29]. Moon [25] carried out two-dimensional (2D) numerical analyses to model cracking in materials composed of non-shrinking aggregates of different shapes embedded in a shrinking cement paste matrix, and found that damage (microcracking) tends to localize around the largest aggregates. Idiart [29,30] studied the effect of aggregate size and volume fraction on drying-induced microcracking, and qualitatively compared the numerical simulations with experimental results. The hygro-mechanical model results showed larger degrees of internal microcracking for higher levels of drying as well as for increasing aggregate volume fraction and size. Grassl et al [28] studied internal microcracking by means of a lattice model on 2D composites with circular aggregates. They found that the average crack width increased with increasing aggregate size and decreased with increasing aggregate volume fraction, whereas the crack density showed opposite trends.

A more realistic modeling approach would be to perform simulations and experiments in three dimensions (3D), explicitly considering the effects of non-uniform drying. However, a deterministic simulation of such 3D experimental tests would require a precise 3D spatial distribution of the aggregates in the model, which is difficult to obtain (see e.g., [31]). Furthermore, the 3D model must then be considerably more sophisticated than the 2D one proposed here, since it needs to consider moisture transport coupled to shrinkage, and the computational cost is considerably higher [32]. Alternatively, aggregate-induced microcracking due to uniform autogenous shrinkage of the matrix can be studied as in [20,33]. However, since in this case the (micro)cracking occurs during the (early) hydration process, the numerical simulations need to take into account the development of shrinkage, mechanical properties and creep as function of the degree of hydration [33].

Since detection of (sub-)microcracks inside real concrete is cumbersome, numerical modeling potentially offers an effective way to investigate and predict aggregate-induced desiccation microcracking. In this paper a procedure is described to quantitatively calibrate hygro-mechanical concrete models by using experimental samples with simplified and approximately matching spatial aggregate distributions. It is noted that the principles and challenges of making a quantitative numerical–experimental comparison, which is the main aim of this paper, are expected to be largely similar for the 2D and 3D cases. As an example, the numerical model calibrated in this work is used to predict, for specific conditions, the critical aggregate size below which aggregate-restraint does not cause detectable microcracking.

2. Experimental methods

2.1. Sample preparation

The experiment was designed to produce 2D crack-patterns in order to facilitate comparison with the 2D numerical simulations. By preparing thin samples and applying a relatively slow drying rate, it was attempted to avoid or minimize the formation of cracks due to non-uniform drying [34,35]. Furthermore, the real and simulated 2D composites contained approximately matching mono-sized aggregate spatial distributions. Two aggregate distributions were numerically generated (as described in Section 3.1) with 10 and 35% aggregate volume fractions, corresponding to 15 and 53 aggregates per sample, respectively. Four different aggregate sizes were studied: 2, 3, 4, and 6 mm diameter (see exact dimensions in Table 1). It is noted that the size of the samples is scaled so that the geometry (and thus the number of aggregates) is identical in samples with the same volume fraction and different aggregate sizes. The aggregates were 2.2 mm-thick slices cut from stainless steel rods. Before being sliced, the rods were roughened by grit-120 grinding paper to increase the bond with the cement paste. The inclusions were glued onto a transparency with a print of the random aggregate distribution with a size scaled to aggregate size (see Section 3.1) and then placed in molds. Three samples per case were tested.

Table 1
Sample catalog.

Sample	Aggr. size (mm)	Aggr. fract. (%)	Sample size (mm)	Ave. thickness ± st. dev. (mm)	n
2 mm–10%	1.98	10	21.5×21.5	1.61±0.080	3
3 mm–10%	2.97	10	32.4×32.4	1.96±0.030	3
4 mm–10%	3.98	10	43.3×43.3	1.96±0.014	3
4 mm–35%	3.98	35	43.3×43.3	2.03±0.003	3
6 mm–10%	5.97	10	65.0×65.0	2.00±0.027	3

Experimental and simulated samples were compared to determine the spatial mismatch of the aggregate distributions. To this end, binary images of the aggregates in the experimental samples were produced, and the coordinates of the aggregate center were compared with the simulated ones. In this way, the average mismatch was found to be between 200 and 300 μm in all samples, corresponding to a relative mismatch (normalized with aggregate size) of around 10% to 5% in samples with 2 to 6 mm aggregates, respectively.

The matrix consisted of <63 μm filtered Portland cement (CEM I 52.5 R) with an added w/c ratio of 0.5. The paste was poured into the molds to a height of about 1 cm and vibrated briefly. The samples were taken out of the molds after 24 hours of sealed-curing and placed in a Ca-saturated solution for another 27 days. After 1 week of wet-curing the samples were wet-ground from their top surfaces to a thickness of about 2.2 mm. At an age of 27 days the samples were further fine-ground in lime-saturated water to a thickness of around 2 mm (see Table 1). Additional samples ($8\times8\times20$ mm^3) of the same cement paste were prepared for measuring compressive strength and Young's modulus of the saturated matrix material in the composites at an age of 28 days.

The drying tests were started at a sample age of 28 days and were carried out in a climate chamber (Vötsch VC4060) at 20±0.2 °C. Samples were placed on a grid and dried from the two faces, while the 2 mm-thick sample edges were covered with layers of adhesive tape. All samples were ultimately dried to 60% relative humidity (RH), i.e., until they reached a constant sample mass. In order to reduce the development of sharp moisture gradients, the following stepwise drying procedure was used: 1 day at 95% RH; 3 days at 80% RH; 3 days at 70% RH; and 31 days at 60% RH. The attempts to completely avoid surface cracking induced by non-uniform drying were not successful in this study (see next section).

2.2. Crack-pattern analyses

After drying, the samples were removed from the climate chamber and directly submerged in an epoxy-resin bath containing a fluorescent dye. The low-viscosity resin entered the cracks by capillary suction, i.e., no vacuum-suction was applied to avoid additional shrinkage cracking in the samples. In a previous study, 'passive' capillary suction led to a reduction of impregnated microcracks of 20% in 4 cm-thick samples compared to vacuum-impregnation [22]. However, for the 2 mm-thick specimens used in this study it is not expected that the amount of the cracks impregnated by capillary suction differs significantly from the one under vacuum impregnation. After 20 min, the samples were taken out from the resin bath and placed on aluminum foil with some excess resin poured over the samples. After hardening of the epoxy,

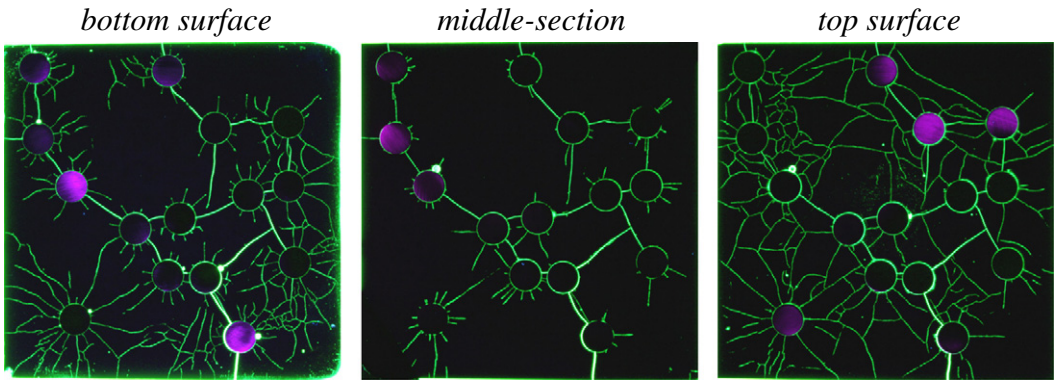

Fig. 1. Crack-patterns of top, middle, and bottom sections in 6 mm–10% sample (65×65 mm^2). Top and bottom surfaces show a significant amount of cracks induced by non-uniform drying.

the excess epoxy on both drying surfaces was removed by grinding. The surfaces were finished by fine grinding on grit-1000 paper. The crack-patterns on both sides of the samples were photographed in fluorescent light with long exposure times using an 8 Mpix digital camera (Fig. 1). Subsequently, one side of the samples was strengthened by a thick layer of araldite glue and ~1 mm of material was ground away from the other sample side to expose the crack-pattern in the sample center, which was then photographed (Fig. 1).

Experimental and simulated crack-patterns were analyzed in exactly the same manner. First, the images were resized to 2500×2500 pixels. Then, cracks and aggregates were traced manually to obtain binary crack-maps with one-pixel wide cracks (Fig. 2). Debonding cracks between aggregates and matrix were not mapped, because their occurrence in experiments is hard to judge for a number of reasons [22]. Top and bottom surfaces showed a significant amount of cracks caused by non-uniform drying (Fig. 1), forming cellular patterns away from aggregates and with a penetration depth of less than 500 μm. To exclude these cracks, two types of experimental crack-patterns were analyzed: (i) crack-patterns as observed in the middle-section of samples (Fig. 1); and (ii) patterns of cracks penetrating the complete sample from top to bottom surface, from now on denoted as *through-going* cracks. The through-going crack-patterns were obtained by stacking the binary crack-pattern images of the bottom, top and middle-section surfaces and deleting all non-overlapping cracks. This stacking procedure also revealed that all cracks are approximately perpendicular to the drying surface and that crack-branching with depth did not occur.

Three different crack-pattern measures were used to quantitatively compare the experimental and simulated results: (i) crack length per unit area (cm/cm^2); (ii) average number of radial cracks per inclusion perimeter length; and (iii) overall crack orientations. The crack length was measured with Matlab as the length of line segments going through the middle points of crack pixels. These are approximate lengths because the cracks were traced on low resolution images, thus ignoring microscale roughness (see Fig. 2), and there is a (maximum) digitalization error of 5% associated with the used method [22]. The crack orientation was measured in Matlab using the function *regionprops*. In order to use this function, curved cracks were subdivided into straight segments by removing crack-pixels, resulting in a reduction of total crack length by 2–5%. The orientation of all crack segments were plotted in radar diagrams using a bin size of 30°.

3. Description of the numerical model

3.1. Random geometry and mesh generation

The numerical model considers a 2-phase composite with circular mono-sized aggregates embedded in a homogeneous matrix. Two random geometries containing 10% and 35% aggregate volume fraction were generated. The position of each inclusion was determined by a pseudo-random number for each coordinate of the inclusion center (C^i_x, C^i_y) as:

$$C^i_x = Ran_x \cdot L, \quad C^i_y = Ran_y \cdot L \tag{1}$$

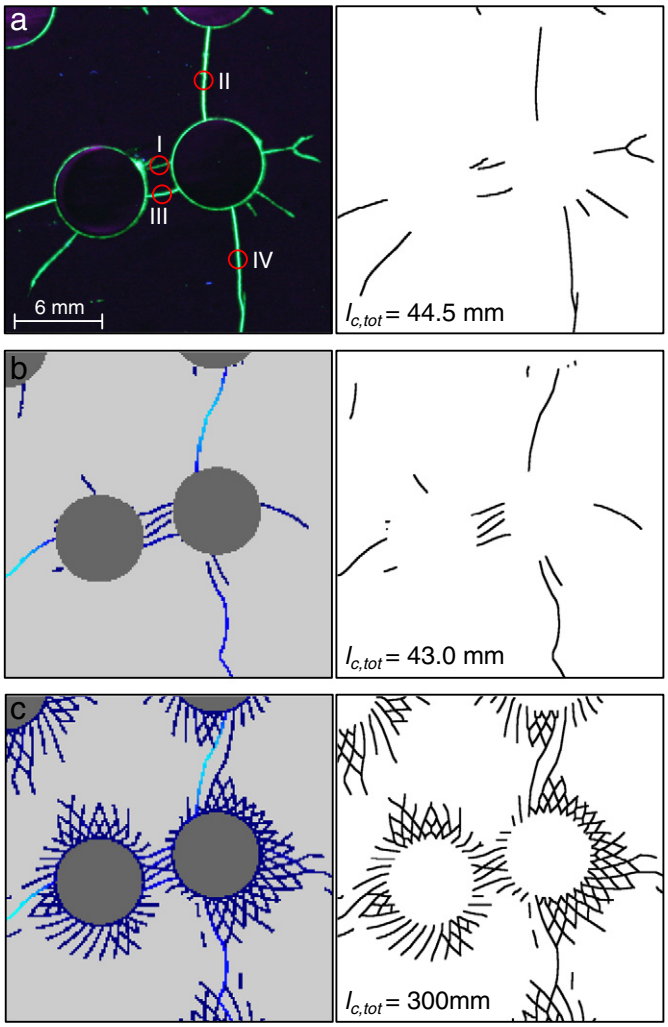

Fig. 2. Example of crack-maps in 6 mm–10% samples: (a) experimental middle-section crack-pattern (roman numbers indicate cracks shown in Fig. 5); (b) simulated crack-pattern at corresponding sample position (crack width threshold 0.8 μm); and (c) same simulation as in (b) but no crack width threshold applied. The gray (blue) scale in (b) and (c) show the crack width ranging from 0.8 μm and 0.7 nm (darkest), respectively, to 10 μm (brightest).

where Ran_j is the pseudo-random number ($j = x,y$), and L is the dimension of the sample. To avoid aggregate overlapping and establish a minimum distance between aggregate and sample boundaries, two geometrical restrictions were applied:

$$\lambda_x = \lambda_y \geq 0.5 \cdot \gamma \cdot d_{agg}, \quad \lambda_{agg} \geq \gamma \cdot d_{agg} \tag{2}$$

where λ_{agg} is the distance between aggregates centers, λ_x, λ_y are the distances between the aggregate perimeter and the sample boundaries, d_{agg} is the aggregate diameter, and γ is a proximity control parameter (in this study, γ varies from 1.05 to 1.25).

The geometry obtained in this way is meshed with a standard unstructured mesh generation method, considering linear triangular continuum elements. The two meshes finally chosen for this study are depicted in Fig. 3. The same meshes have been used in all the simulations, by considering a rescaling factor depending on the size of the sample. In order to represent cracking, two families of linear zero-thickness interface elements are inserted in the FE mesh: the first one between all the matrix–matrix element contacts, while the other one along all the aggregate–matrix contacts. Steel inclusions did not crack in the experiments, and thus no interface elements were inserted inside the inclusions. Linear elasticity was considered for steel inclusions, with standard elastic properties (see Table 2).

3.2. Modeling of shrinkage and creep

Drying shrinkage of the matrix phase in the 2D-model is assumed uniform, and moisture transport processes that are associated with drying shrinkage in reality are not considered here. Shrinkage of the matrix phase is linked to the moisture state through the shrinkage coefficient, i.e., the slope of the strain vs. relative humidity curve. It has been experimentally shown that this curve is approximately linear for cement pastes with w/c-ratio of 0.4 to 0.5 in the relative humidity range of 40–100% [36,37]. Duckheim and Setzer [36] measured a constant shrinkage coefficient of 0.06 mm/m/%RH in the range of 40–100% RH for a 0.5 w/c-ratio paste. An ultimate shrinkage strain of 5.1 mm/m at 25% RH was measured in [35] for the same cement paste used in this study. Assuming linear behavior in the 25–100% RH range, this corresponds to a shrinkage coefficient of 0.07 mm/m/%RH, which has been adopted for the matrix phase in the model. The higher shrinkage coefficient for our 0.5 w/c-ratio paste may possibly be explained by the finer cement used in this study (CEM I 52.5 R) compared to the CEM I 32.5 R used in [36].

To consider the time-dependent deformations of the matrix phase, i.e., the aging viscoelasticity of hardened cement paste, the model is equipped with a basic creep law. The creep law does not account for nonlinear creep effects produced by microcracking. Instead, cracks are explicitly modeled with the insertion of interface elements so that the creep law in the (uncracked) continuum is approximately linear. The creep model was determined mainly with data on creep under compression, while during drying shrinkage the cement paste is subjected to tensile stresses. However, for well-cured cement pastes, which is the case of this study, creep in tension and compression are essentially similar. It is generally accepted that creep tensile deformation is at least as large as in compression, and sometimes higher (see [38–40] and references therein). Cracking during tensile creep would lead to larger strains compared to creep under compression [39]. However, as already mentioned, microcracking is explicitly accounted for in the present work with the insertion of interface elements to represent potential cracks.

The rheological model consists of an aging Maxwell-chain based on previous work by Bažant and coworkers [41,42]. The determination of the Maxwell-chain parameters for the matrix phase is a difficult task, since experimental data on aging and creep of cement paste is scarce. Therefore, these parameters are calculated by least-squares fit of the chain's response to the prediction of a given creep function [42]. The compliance functions for two different creep laws have been set so that the elastic modulus at 28 days fits the experimentally measured one (12.5 GPa in this study) and that the creep strains for 28 days curing and ~30 years (10,000 days) of loading are either 2 or 4 times the initial elastic strain. For the duration of drying in the present experiments (38 days), these values are respectively 1.3 and 2. The creep laws considered here are only estimates based on creep strains measured on similar cement pastes (high early strength Portland cement with w/c-ratio of 0.53) [43]. The high-creep compliance function used here corresponds approximately to the one measured in [43] (high early strength Portland cement is known to creep more than normal cement), while the moderate-creep law was

Table 2
Model parameters used in simulations.

Continuum elements		
$E_{t\text{-}28d}$		Aging Maxwell chain
E_{28d} (GPa); ν_{hcp} (−)		12.5; 0.2
E_{steel} (GPa); ν_{steel} (−)		200; 0.3
Interface elements	matrix–matrix	Inclusion–matrix
χ (MPa)	7.0	1.5
c (MPa)	24.0	5.0
$\tan\phi$	0.6	0.4
$\tan\phi_r$	0.2	0.2
G_F^I (N/mm)	0.01	0.001
G_F^{IIa} (N/mm)	0.1	0.01
σ_{dil} (MPa)	40	40

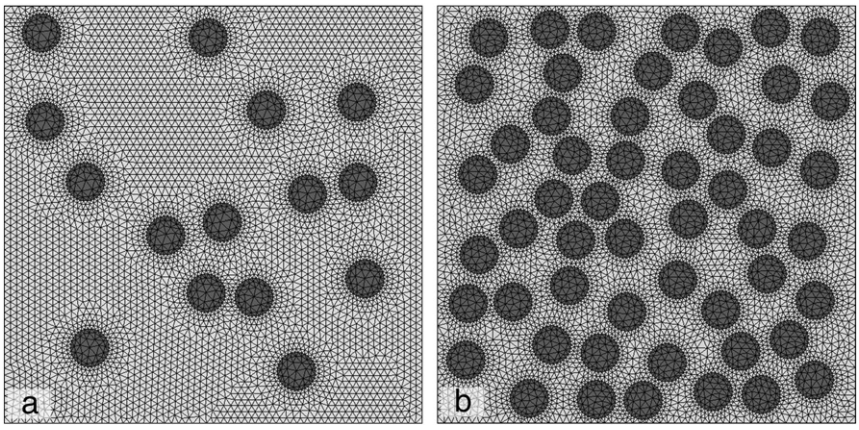

Fig. 3. FE meshes used in the simulations: (a) 10% aggr. volume fraction (15 inclusions, 26,440 nodes, 9750 continuum and 12,912 interface elements) and (b) 35% aggr. volume fraction (53 inclusions, 30,160 nodes, 13,482 continuum and 14,260 interface elements).

considered arbitrarily to yield half of the final strain. The stepwise drying procedure used in the experiments (see Section 2.1) was explicitly taken into account in the simulations. Within each drying step, prescribed shrinkage strains are assumed to be proportional to time. Intrinsic moisture dependence of basic creep (e.g., [44,45]) and of fracture energy (e.g., [46]) was not considered in the model.

3.3. Cohesive fracture model

The constitutive law for interface elements is the key feature of the model, since it enables the simulation of fracture. It is based on the model developed in [47–49], where a detailed description can be found. In the following only the fundamentals of the model are summarized. The law is formulated in terms of the normal and tangential stress components on the mid-plane of the joint (σ_N and σ_T) and the corresponding relative displacements (u_N and u_T). It is based on the theory of elasto-plasticity and introduces nonlinear Fracture Mechanics concepts [29,32,47–49]. The elastic stiffness matrix is diagonal and the elastic constants can be regarded simply as penalty coefficients (meaning that their values should be as high as possible, see e.g. [30,48]). The fracture surface $F(\sigma,p)=0$ is represented by a hyperbola in the stress-traction space, which in its simplest expression might be defined by three independent parameters (p): tensile strength χ, apparent cohesion c and asymptotic friction angle ϕ. The fracture surface is shown as curve 0 in Fig. 4 and is given by:

$$F = \sigma_T^2 - (c - \sigma_N \cdot \tan\phi)^2 + (c - \chi \cdot \tan\phi)^2 = 0 \quad (3)$$

Cracking starts as soon as the fracture surface is reached. Softening is controlled by the shrinkage of the failure surface due to the decrease of parameters p, which evolve according to the work spent during the fracture process, denoted by W^{cr} (see Fig. 4). In this work, a linear softening law for each of the parameters has been considered. The model introduces two additional parameters: the fracture energy in mode I, G_F^I (pure tension), and the fracture energy in mode IIa, denoted as G_F^{IIa}, defined by a shear state under a high enough compression level so that dilatancy is prevented (see [48]). In this way, the total exhaustion of the tensile strength ($\chi=0$) is reached when $W^{cr}=G_F^I$ (curve 1 in Fig. 4), and the residual friction state ($c=0$ and $\tan\phi=\tan\phi_r$) is attained when $W^{cr}=G_F^{IIa}$ (curve 2 in Fig. 4). A non-associated plastic potential Q is adopted (i.e. $Q\neq F$) in order to progressively eliminate dilatancy for high levels of compression (dilatancy vanishes progressively for $\sigma_N \to \sigma_{dil}$). The dilatancy angle also degrades during the fracture process, vanishing when $W^{cr}=G_F^{IIa}$. Even though not all the parameters are known a priori, some of them can be estimated from mechanical tests. The constitutive behavior of the model may be directly compared with experiments to determine some of the parameters (χ, c, ϕ, ϕ_r, G_F^I), as for the cases of uniaxial tensile tests and mixed mode shear/compression tests in concrete in [48–50]. Regarding the rest of parameters (G_F^{IIa}, σ_{dil}), their effect on the overall mechanical response of the specimen has been previously studied extensively. They can be estimated from inverse analysis when fitting the overall response of concrete specimens subject to compression and tension (especially including the softening branch) with a mesostructural model including zero-thickness interface elements [32,49–50].

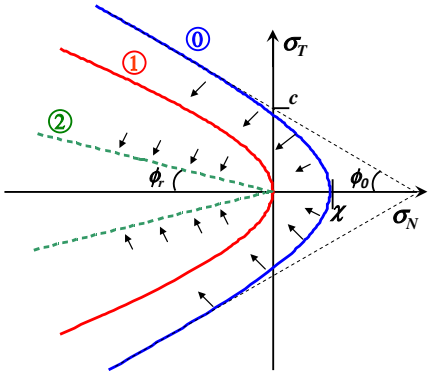

Fig. 4. Fracture surface evolution with increasing work dissipated in fracture process: the initial state is given by curve 0; curve 1 corresponds to the exhaustion of tensile strength; curve 2 corresponds to the final residual state (pure friction). Note also the evolution of the friction angle from ϕ_0 to ϕ_r.

In the present paper, the same constitutive model has been adopted for inclusion–matrix and matrix–matrix interface elements. In the former, the parameters are chosen such that tensile strength is very small (1.5 MPa) and only friction under shear/compression stresses is relevant. For the latter, tensile strength of 7 MPa and friction with small dilatancy angle have been adopted. Tensile strength was assumed to be 10% of the 28-day compressive strength that was measured experimentally; tensile strength of cementitious materials is between 7 and 11% of the compressive strength [51]. Selected simulations were repeated for tensile strengths of 6 and 8 MPa in order to test the sensitivity of the model to this parameter. Model parameters used in the simulations for both types of interface elements are gathered in Table 2. Note that the choice of the bond strength in the model may have an influence on aggregate-induced shrinkage cracking [20,22]. Future comparative simulations could certainly benefit from the direct measurements of tensile strengths of the matrix phase and the matrix–aggregate bond.

Crack-patterns obtained with the present model, as well as with other meso-mechanical models applied to the particular case of cracking due to aggregate-restraint (see e.g. [21,27–30]), have shown spurious cracks around the aggregates (see Fig. 2c). These cracks are characterized by their very small width on the nanometer scale. Generation of these apparently artificial nano-cracks may be due to different reasons, like mesh-dependency effects, a lack of heterogeneity of the main material properties, or the way in which shrinkage is simulated, typically as uniformly imposed volumetric strains. In order to be able to quantitatively compare experimental and numerical crack-patterns, crack-width filtering of the crack-pattern was carried out as a post-process. To study the sensitivity of the crack-patterns on this filtering, crack width filtering thresholds of 0, 0.5, 0.8, and 1 μm were used, as motivated in Section 4.1. This corresponds to excluding cracks in which 0, 3.3, 5.3, and 6.6% of G_F^I was dissipated, respectively.

4. Results

4.1. Crack widths

The experimental impregnated crack widths observed in this study (on middle sections) mainly ranged between 0.5 and 50 μm, but occasionally were above 100 μm at the sample edges. The lower detection limit of cracks is not determined by the resolution of the camera lens or microscope, but depends primarily on the ability of the epoxy resin to penetrate the smaller cracks. It is not clear whether the thinnest impregnated cracks observed in this study (about 0.5 μm) represent the impregnation limit or the actual thinnest cracks present in the samples. This would have to be determined by another technique capable of detecting cracks in cement paste with widths in the range of 10's to 100's of nanometers.

High magnification images of selected cracks in Fig. 2 are shown in Fig. 5. The widths range between 3 and 35 μm. At some locations, direct comparison of the experimental and simulated crack widths appears to be justified, because the cracks occur at approximately the same location and there are no other cracks in the proximity. At locations II and IV, the simulated widths are 10 and 4 μm, respectively, i.e., a factor 3.5 to 5 smaller than the experimental ones. In between the two central aggregates, the width of the four simulated cracks range from 1.5 to 2.5 μm, while the two experimental widths are 3 and 14 μm. The experimental cracks have a more uniform crack width

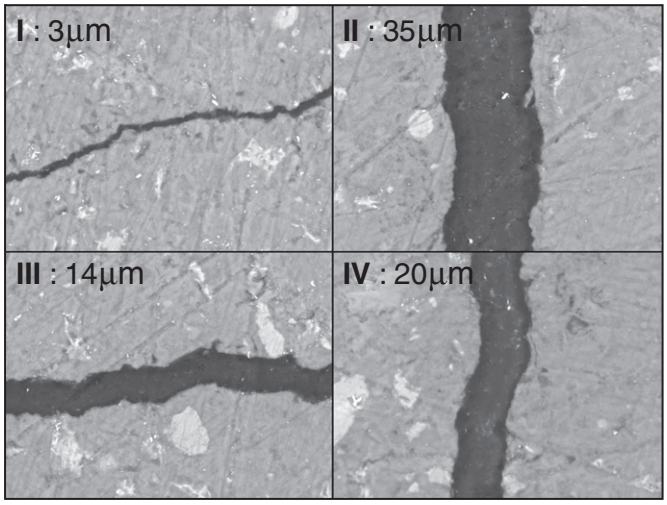

Fig. 5. SEM-BSE images showing width of the epoxy-filled cracks in the 6 mm–10% sample shown in Fig. 2.

along their lengths than the simulated ones, especially those bridging two aggregates. In order to quantitatively compare the experimental and simulated crack-patterns, a crack-filtering threshold needs to be applied as a post-process in the simulations (see Section 3.3). With regard to the experimental detection limit of around 0.5 μm, a sensitivity analysis was conducted using thresholds of 0, 0.5, 0.8 or 1 μm.

4.2. Effect of non-uniform drying in experiments

Before comparing the experimental and simulated crack-patterns, attention is focused to the difference between the two types of experimental crack-patterns, *middle-section* and *through-going*. The latter shows significantly less cracking than the former, as show in Fig. 7 and in the following figures. If all cracks in the samples were caused by aggregate-restraint only, the two types of crack-patterns would be expected to be similar. This is not the case, probably because the top and bottom surfaces showed a significant amount of cracks with a limited penetration depth (Fig. 1). These cracks are most likely caused by non-uniform drying (e.g., [31,35]), despite the fact that the experiments were designed to avoid this type of cracking (see Section 2.1). These 'pre-existing' surface cracks may cause an *offset-growth* of aggregate restraint cracks, as illustrated in Fig. 6. Aggregate-restraint causes pre-existing surface cracks to grow deeper into the sample. If pre-existing cracks only occur on one side of the sample, the aggregate-restraint cracks may become through-going. If, on the other hand, pre-existing cracks happen to occur at similar positions on both sides but with a small offset, they will not grow much beyond the middle section plane. They eventually stop growing, because the two opposing cracks with a small offset can accommodate the same strain as a single through-going crack (as in Fig. 6b, c).

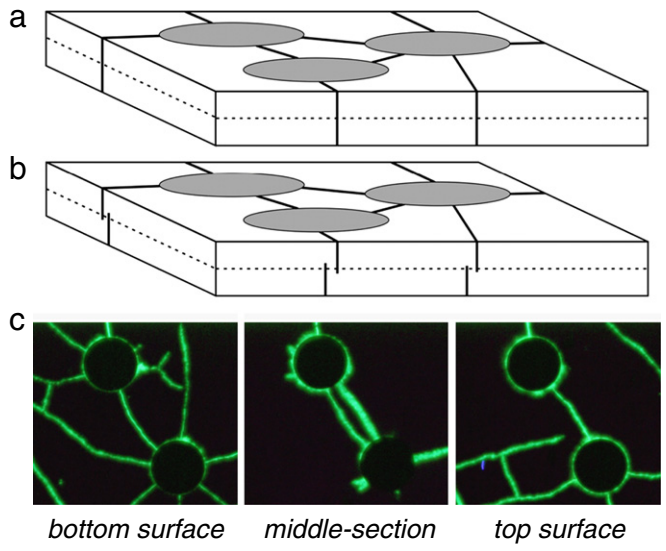

Fig. 6. Effect of non-uniform drying on aggregate-induced desiccation cracking in plate-like specimens. Schematic representation for the case of (a) uniformly and (b) non-uniformly shrinking matrix; (c) Crack-patterns in a 2 mm–10% sample showing crack-doubling on middle-sections due to *offset-growth* caused by non-uniform drying.

The difference in crack length per unit area between the *middle-section* and *through-going* crack-patterns increases with decreasing aggregate size (Figs. 7, 8). This can be explained by the *offset-growth effect* becoming more important in samples with smaller aggregates. This is indicated by the increasing number of parallel bridging cracks on middle sections (as in Figs. 6c, 7) in samples with smaller aggregates (for equivalent volume fraction). These parallel cracks significantly increase the crack length per unit area on these sections.

The offset-growth effect described here does not occur in the 2D simulations. Compared to a hypothetical 2D experimental set-up in which cracks by non-uniform drying would not occur at all, the middle-section patterns probably show too many and the through-going patterns too few cracks. Thus, the two types of experimental crack-patterns may roughly be regarded as upper and lower bounds for 2D aggregate-restraint crack-patterns in this study.

4.3. Quantitative comparison of model and experiment

Experimental and simulated crack-patterns of three selected cases (2 mm–10%, 6 mm–10%, and 4 mm–35% samples) are shown in Fig. 7 for a qualitative comparison. For other samples with 3 mm and 4 mm inclusions, whose crack-patterns show intermediate features, only the quantitative crack-pattern data is given in Figs. 8–10. A similar trend was found between the experimental and simulated crack-patterns with regard to the location of aggregate bridging cracks (Fig. 7), irrespective of the offset-growth effect explained above and independent of the applied crack-filtering threshold or matrix creep level. Simulated 'bridging' cracks never occur between neighboring aggregates that are not crack-bridged in at least one of the three corresponding experimental samples.

In order to make a quantitative comparison between experimental and simulated crack-patterns, an estimate of the magnitude of matrix creep in the model needs to be made first. As explained in Section 3.2, the effect of creep on aggregate-induced cracking was numerically studied for the following cases: (i) no creep, (ii) moderate creep level (i.e., 1.3 times the initial elastic strain at 38 days loading duration); and (iii) high creep level (i.e., 2 times the initial elastic strain at 38 days loading duration). For sample 4 mm–35%, simulated crack lengths per unit area for these three cases using a crack-filtering threshold of 0.5 μm are plotted in Fig. 8b. Labels C1, C2 and C3 in Fig. 8b refer to simulated crack lengths per unit area with no, moderate, or high creep values, respectively. The simulated crack length per unit area for the high-creep case (C3) seems to best agree with the experimental data. However, applying the same creep level for the other sample types leads to a too small crack length per unit area as compared with experiments. For example, in the 6 mm–10% sample, it only represents 40% of the experimental lower-bound value using a crack-filtering threshold of 0.5 μm (high-creep case for 6 mm–10% in Fig. 8a is given by C4). The *no-creep* simulations (with a 0.5 μm threshold) produced crack densities, and especially radial crack numbers, that seem to be too high for the composites with 4 and 6 mm aggregates with regard to the experimental upper-bound values. The moderate creep strain case seems to yield the best overall agreement for the samples in this study and therefore has been used in the

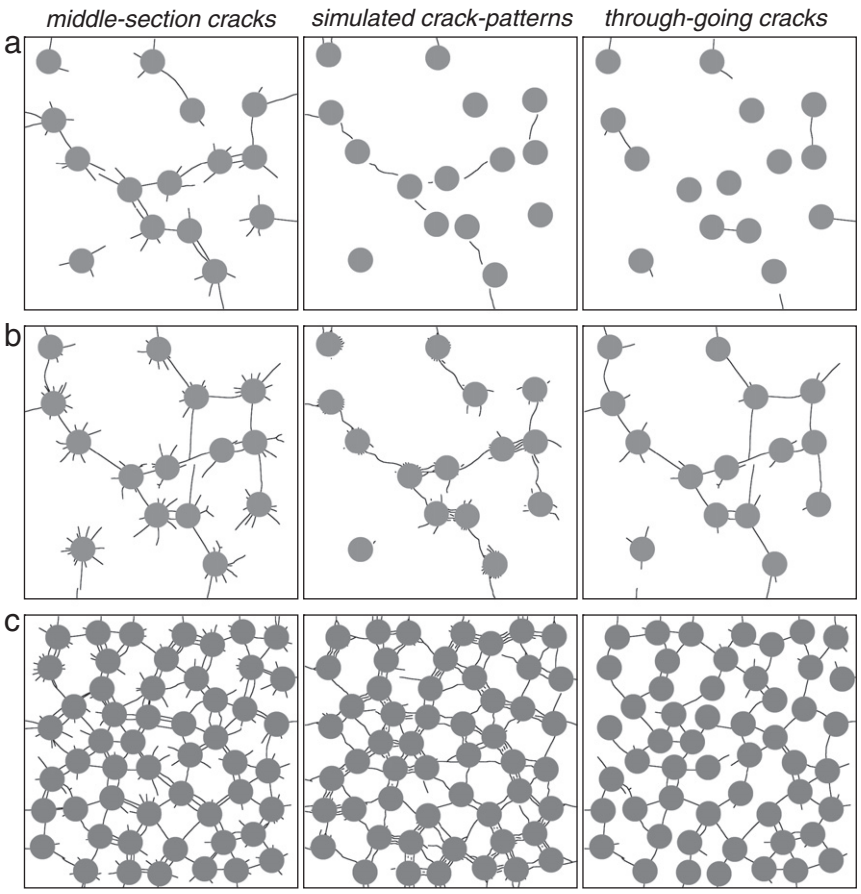

Fig. 7. Qualitative comparison of experimental and simulated (t = 0.8 μm, moderate creep) crack-patterns for the samples (a) 2 mm–10%; (b) 6 mm–10%; (c) 4 mm–35% (see Table 1 for dimensions).

following to quantitatively compare simulated and experimental crack-patterns.

A sensitivity analysis of the effect of the crack-width threshold on the crack-patterns was conducted considering the cases of a 0, 0.5, 0.8 and 1.0 μm threshold. The case of no (zero) threshold produced crack lengths per unit area that are almost an order of magnitude larger than the experimental ones (see Fig. 2), and therefore was not further considered. For a crack-width threshold of 0.5 μm, the simulated results fall in between the two experimental curves in the case of samples containing 10% aggregates. For 35% aggregates this threshold

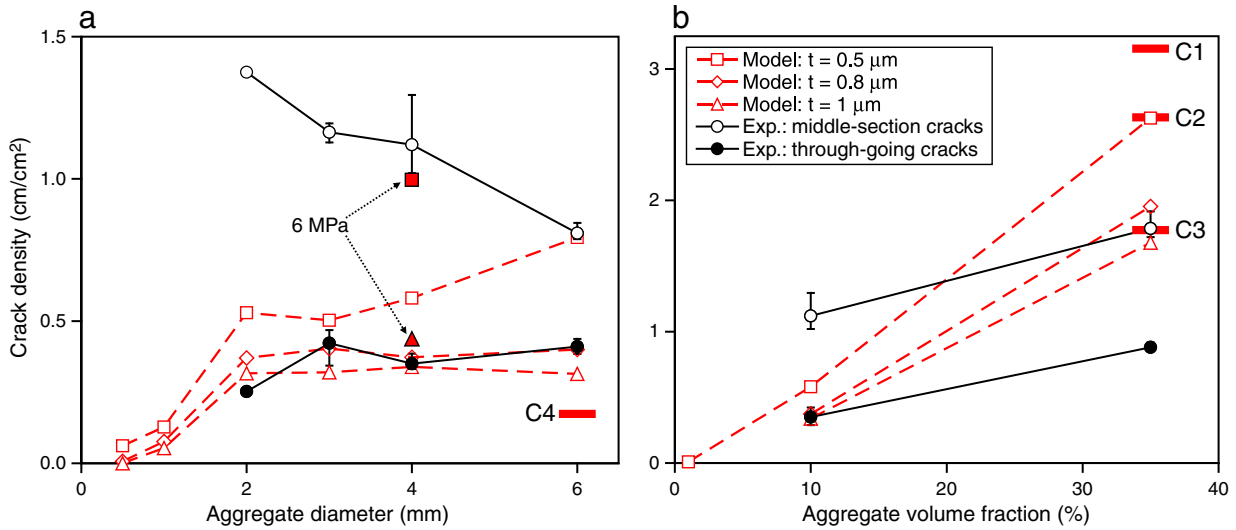

Fig. 8. Crack length per unit area (cm/cm^2) of experimental and simulated crack-patterns (with moderate creep and a tensile strength of 7 MPa) as a function of: (a) aggregate size (for 10% aggregate volume fraction), and (b) aggregate volume fraction (with 4-mm aggregates). Error bars of experimental data show the maximum and minimum values of 3 samples. The meaning of C1–C4 is explained in the text. The result of a simulation using a tensile strength of 6 MPa is also shown (square: t = 0.8; triangle: t = 1.0 μm).

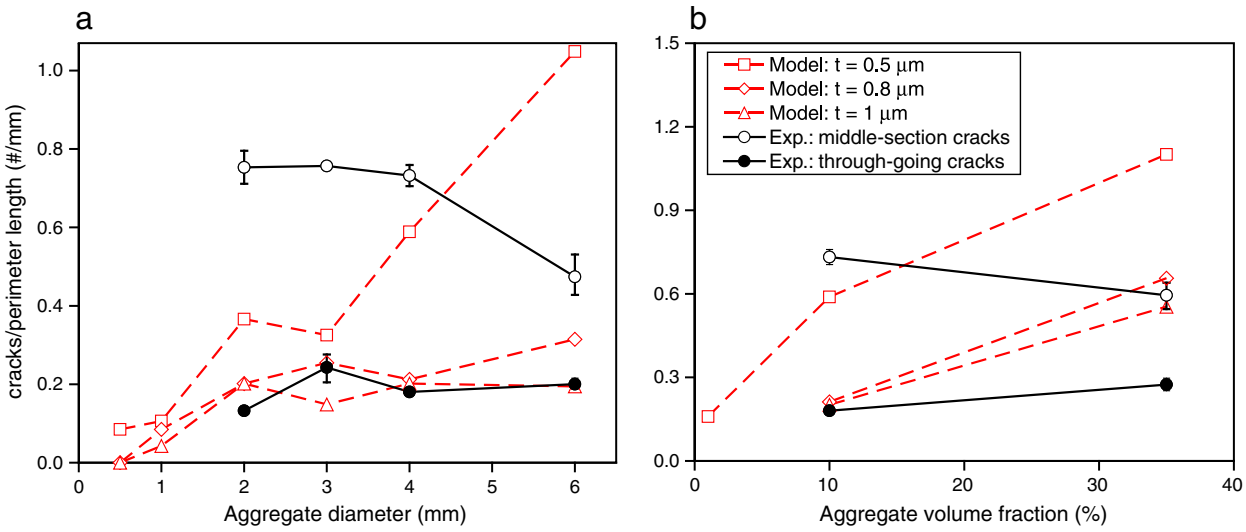

Fig. 9. Number of radial cracks per inclusion perimeter length in experimental and simulated crack-patterns as function of: (a) aggregate size (for 10% aggregate volume fraction), and (b) aggregate volume fraction (4-mm aggregates). Error bars of experimental data show the maximum and minimum values of 3 samples.

seems to yield too many cracks in the simulations. A threshold of 0.8 or 1 μm gives a better agreement for 4 mm–35% samples, and makes other sample types overlap the experimental curve for through-going crack-patterns (Fig. 8). Irrespective of the applied threshold, the trends of crack length per unit area as a function of aggregate size and aggregate volume fraction agree with the experimental observations. It either remains constant or increases as function of aggregate size, and increases with aggregate volume fraction. The only exception is for sample middle-sections, for which crack length per unit area decreases with increasing aggregate size. The latter trend is probably caused, or at least significantly strengthened, by the *off-set-growth* effect described in Section 4.2.

Simulations were also carried out for different values of tensile strength of the matrix phase. For example, by using a tensile strength of 6 MPa instead of 7 MPa, significantly higher crack densities are obtained, and especially for a lower crack filter threshold value (see Fig. 8). This shows the importance of accurately knowing the tensile strength of the matrix phase as an input parameter for the model.

The average number of radial cracks per aggregate perimeter length seems to be only weakly dependent on aggregate size in both experiments and simulations for aggregate sizes above 2 mm and threshold values of 0.8 and 1 μm (Fig. 9). The number of radial cracks per perimeter length increases with aggregate volume fraction in the simulations; however, this trend is not clearly observed in the experiments. It should be noted that the error bars in Fig. 9 show the variation in the average number of radial cracks between samples. The standard deviation of radial crack number in a single sample is much larger, as can be seen in Fig. 7.

4.4. Crack orientation

Regarding the overall crack-pattern orientation, experiments and simulations show similar trends, as depicted in Fig. 10. This shows that preferred elementary orientations in the FE meshes did not significantly affect the overall crack orientations in the simulations. The samples containing 10% aggregates show preferred cracking in the 0–30° and 90–120° directions independent of the aggregate size. Samples containing 35% aggregates show significantly more isotropic crack-patterns, with a slight preferred cracking in the 0° and 60° directions (more pronounced in the simulations than in the experiments). The observed anisotropy in crack orientation is probably a result of the low number of randomly placed aggregates in the samples, and the fact that radial cracks preferably develop along the shortest lines connecting neighboring aggregates (Fig. 7). Randomly distributed aggregates should produce randomly-oriented radial cracks in a sufficiently large volume, which would lead to a circular rose diagram (e.g. [22]). Thus, crack orientations in this study are not representative of large samples of the given mixtures, but are nevertheless useful for comparing experiments and simulations on the same samples.

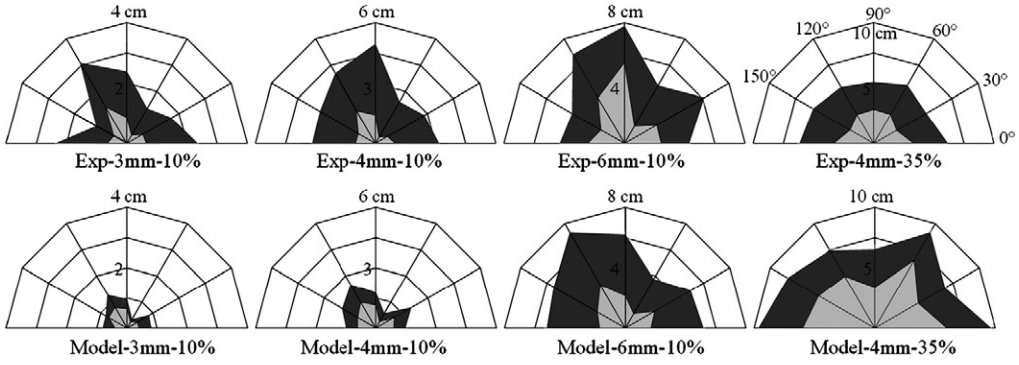

Fig. 10. Crack orientation distributions of the experimental (top) and simulated (bottom) crack-patterns (bin size = 30°). For the experimental diagrams (average of 3 samples): light gray = through-going cracks; dark gray = middle-section cracks. For the model diagrams: light gray = 1 μm crack width threshold; dark gray = 0.5 μm crack width threshold.

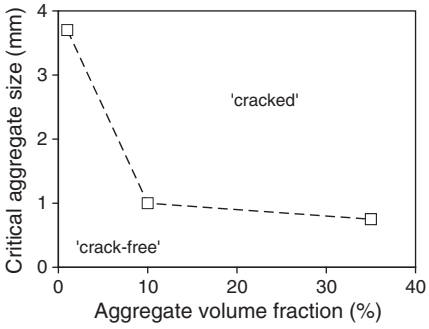

Fig. 11. Model predicted critical aggregate size for cementitious composites with mono-sized steel inclusions (dried to 60% RH; moderate creep of matrix) for 1, 10 and 35% volume fraction. Crack-free means no desiccation cracks with a modeled width >0.5 μm.

The anisotropy in simulated crack-patterns is largely unaffected by the crack filtering threshold in the 3 and 4 mm–10% samples. In the 6 mm–10% and 4 mm–35% samples, the anisotropy decreases at lower crack-filtering threshold, due to the inclusion of more randomly-oriented radial cracks in the plots as the threshold is decreased. In the case of 6 mm samples, these are short, non-bridging radial cracks. On the experimental side, the middle-section crack-patterns are less anisotropic than the through-going crack-patterns, due to the presence of shorter randomly oriented radial cracks in the former (Fig. 7).

5. Discussion

In this paper, a procedure is described to calibrate a simplified 2D numerical model for concrete using 2D experiments with approximately matching spatial aggregate distributions. A well-calibrated 2D numerical model should be able to make predictions about desiccation microcracking for 'real' concretes with practical aggregate size distributions and volume fractions. The final objective is the formulation and experimental calibration of a 3D hygro-mechanical model, including moisture transport. However, the principles and challenges of making a quantitative simulation–experiment comparison, which this paper is aiming to describe, are expected to be largely the same for the 3D case.

As a practical application, a calibrated model could also be used to determine if a critical aggregate size for aggregate-induced desiccation cracking in real concretes exists. Experimental and numerical results (for thresholds of 0.8 and 1 μm) show that above an aggregate size of 2 mm, the average number of radial cracks per perimeter length is not strongly dependent on aggregate size (Fig. 9). In other words, the spacing between radial cracks around aggregates remains approximately constant above an aggregate size of 2 mm. This result suggests the existence of a critical aggregate size in the case of aggregates embedded in a shrinking matrix: when the aggregate perimeter length approaches the radial crack spacing distance, no crack at all, or a minimum number of radial cracks will form with a width that possibly is too small to be experimentally detected. This observation can be compared with shrinkage cracks in a concrete repair layer showing an approximately constant crack-spacing: if the length of the repair layer approaches the crack-spacing distance, no cracking will occur. The case of this study is of course more complicated, but at least it explains why the number of radial cracks along the perimeter of an aggregate increases with aggregate size.

In this study, the calibrated model has been used to predict critical aggregate sizes (with crack widths below a modeled threshold of 0.5 μm), in cementitious composites with mono-sized steel inclusions having a random spatial distribution. Results are depicted in Fig. 11 (the results for the case with 1% volume fraction were obtained with a mesh considering one single inclusion embedded in a large matrix phase). These predictions should of course be taken with caution, because of the underlying assumptions of the model and the experimental limitations. It is predicted that the critical aggregate size increases with decreasing aggregate volume fraction, especially in highly diluted mixtures with less than 10% aggregates (Fig. 11). Above 10% aggregates, the critical aggregate size decreases only slightly with increasing aggregate volume fraction. This result suggests that in meso-scale concrete models, the sand particles <1 mm cause negligible microcracking upon drying (under the material composition and drying conditions considered in this study). Therefore, this sand fraction could in principle be homogenized in an effective matrix that considers cement paste and small particles as a homogeneous phase with transport and mechanical effective properties (see e.g. [52,53] for details on homogenization approaches). If small inclusions were not needed to be explicitly modeled, the computation time for modeling aggregate-induced desiccation cracking in concrete would be greatly reduced.

6. Conclusions

As shown in this paper, the main challenges of performing a quantitative comparison of experiments with a 2D meso-mechanical model for shrinkage cracking in cementitious materials are: (1) designing an experiment with no or negligible effects of drying-induced moisture gradients. (2) Knowing the actual basic creep response of the matrix phase. As shown, overall agreement of experimental and simulated crack-patterns was better when creep strains of the cement paste matrix (i.e., stress-relaxation of drying-induced stresses) were considered in the numerical model. In this regard, future simulations would benefit from using an experimentally measured creep compliance function of the cement paste matrix. (3) Determining what proportion of the simulated cracks has a width that is below the experimental detection limit.

The experimental and calibrated model results seem to show that the aggregate-induced crack density upon drying increases with aggregate size and volume fraction. The normalized number of radial cracks around aggregates shows more or less the same trends as function of these variables, indicating that this parameter is proportional to the crack density. The overall orientation of cracks of the simulated crack-patterns agreed well with the experimental results in this study. The results obtained suggest that there is a critical aggregate size below which aggregate-restraint does not cause experimentally detectable microcracks. The model predicts that this critical aggregate size decreases with increasing aggregate volume fraction.

References

[1] R.W. Carlson, Drying shrinkage of concrete as affected by many factors, Proc. of the American Society for Testing Materials, Part 2, 38, 1939, pp. 419–437.
[2] D.W. Hobbs, Influence of aggregate restraint on the shrinkage of concrete, ACI J. 71 (1974) 445–450.
[3] A.M. Neville, Properties of Concrete, 4th edition Pearson Prentice Hall, 2002.
[4] P. Goltermann, Mechanical predictions of concrete deterioration — part 2: classification of crack patterns, ACI Mater. J. 92 (1995) 58–63.
[5] V. Kanna, R. Olson, H. Jennings, Effect of shrinkage and moisture content on the physical characteristics of blended cement mortars, Cem. Concr. Res. 28 (1998) 1467–1477.
[6] I. Yurtdas, N. Burlion, F. Skoczylas, Triaxial mechanical behaviour of mortar: effects of drying, Cem. Concr. Res. 34 (2004) 1131–1143.
[7] N. Burlion, F. Bourgeois, J. Shao, Effects of desiccation on mechanical behaviour of concrete, Cem. Concr. Comp. 27 (2005) 367–379.
[8] C. Aldea, S.P. Shah, A. Karr, Effect of cracking on water and chloride permeability of concrete, ASCE J. Mater. Civil Eng. 11 (1999) 181–187.
[9] A. Djerbi, S. Bonnet, A. Khelidj, V. Baroghel-Bouny, Influence of traversing crack on chloride diffusion into concrete, Cem. Concr. Res. 38 (2008) 877–883.
[10] M. Ismail, A. Toumi, R. François, R. Gagné, Effect of crack opening on the local diffusion of chloride in cracked mortar samples, Cem. Concr. Res. 38 (2008) 1106–1111.
[11] H.S. Wong, M. Zobel, N.R. Buenfeld, R.W. Zimmerman, The influence of the interfacial transition zone and microcracking on the diffusivity, permeability and sorptivity of cement-based materials after drying, Mag. Concr. Res. 61 (2009) 571–589.
[12] A.E. Idiart, C.M. López, I. Carol, Chemo-mechanical analysis of concrete cracking and degradation due to external sulfate attack: a meso-scale model, Cem. Concr. Comp. 33 (3) (2011) 411–423.

[13] J. Bisschop, J.G.M. van Mier, How to study drying shrinkage microcracking in cement-based materials using optical and scanning electron microscopy? Cem. Concr. Res. 32 (2002) 279–287.
[14] K.O. Kjellsen, H.M. Jennings, Observations of microcracking in cement paste upon drying and rewetting by environmental scanning electron microscopy, Adv. Cem. Based Mater. 3 (1996) 14–19.
[15] J. Bisschop, J.G.M. van Mier, Environmental scanning electron microscopy as tool to study shrinkage microcracks in cement-based materials, Proc. of MRS 1999 Fall Meeting, Boston, Advances in materials problem solving with the electron microscope, vol. 589, 2000, pp. 141–146.
[16] H.C. Gran, Fluorescent liquid replacement technique. A means of crack detection and water: binder ratio determination in high strength concretes, Cem. Concr. Res. 25 (1995) 1063–1074.
[17] T.T. Hsu, Mathematical analysis of shrinkage stresses in a model of hardened concrete, J. ACI 60 (1963) 371–390.
[18] D.R. McCreath, J.B. Newman, K. Newman, The influence of aggregate particles on the local strain distribution and fracture mechanism of cement paste during drying shrinkage, Mater. Struct. 2 (1969) 73–85.
[19] N. Hearn, Effect of shrinkage and load-induced cracking on water permeability of concrete, ACI Mater. J. 96 (1999) 234–241.
[20] B. Dela, H. Stang, Two-dimensional analysis of crack formation around aggregates in high-shrinkage cement paste, Eng. Fract. Mech. 65 (2000) 149–164.
[21] F. Lagier, X. Jourdain, C. De Sa, F. Benboudjema, J.B. Colliat, Numerical strategies for prediction of drying cracks in heterogenous materials: comparison upon experimental results, Eng. Struct. 33 (2011) 920–931.
[22] J. Bisschop, Drying shrinkage microcracking in cement-based materials. PhD-thesis Delft Univ. of Tech., Delft Univ. Press 2002, The Netherlands (ISBN 90-407-2341-9).
[23] J. Bisschop, J.G.M. van Mier, Effect of aggregates on drying shrinkage microcracking in cement-based materials, Mater. Struct. 35 (2002) 453–461.
[24] P.E. Roelfstra, A numerical approach to investigate the properties of concrete: numerical concrete. PhD Thesis EPFL, Lausanne, Switzerland, 1989, 199 p.
[25] J.H. Moon. Shrinkage, Residual Stress, and Cracking in Heterogeneous Materials. PhD thesis, Purdue University, West Lafayette, Indiana, May 2006.
[26] E. Schlangen, E.A.B. Koenders, K. van Breugel, Influences of internal dilation on the fracture behaviour of multi-phase materials, Eng. Fract. Mech. 740 (2007) 18–33.
[27] J.X. Liu, Z.Y. Zhao, S.C. Deng, N.G. Liang, A simple method to simulate shrinkage-induced cracking in cement-based composites by lattice-type modeling, Comput. Mech. 43 (2009) 477–492.
[28] P. Grassl, H.S. Wong, N.R. Buenfeld, Influence of aggregate size and volume fraction on shrinkage induced micro-cracking of concrete and mortar, Cem. Concr. Res. 40 (2010) 85–93.
[29] A.E. Idiart, C.M. López, I. Carol, Modeling of drying shrinkage of concrete specimens at the meso-level, Mater. Struct. 44 (2) (2011) 415–435.
[30] A.E. Idiart, Coupled analysis of degradation processes in concrete specimens at the meso-level. PhD thesis, UPC, Barcelona, Spain, 2009.
[31] H.K. Man, J.G.M. van Mier, Size effect on strength and fracture energy for numerical concrete with realistic aggregate shapes, Int. J. Fract. 154 (2008) 61–72.
[32] A. Caballero, I. Carol, C.M. López, 3D meso-mechanical analysis of concrete specimens under biaxial loading, Fatigue Fract. Eng. Mater. Struct. 30 (2007) 877–886.
[33] P. Lura, O.M. Jensen, J. Weiss, Cracking in cement paste induced by autogenous shrinkage, Mater. Struct. 42 (2009) 1089–1099.
[34] Z.P. Bažant, W.J. Raftshol, Effect of cracking in drying and shrinkage specimens, Cem. Concr. Res. 12 (1982) 209–226.
[35] J. Bisschop, F. Wittel, Contraction gradient induced microcracking in hardened cement paste, Cem. Concr. Comp. 33 (2011) 466–473.
[36] C. Duckheim, M.J. Setzer, Drying shrinkage mechanisms of hardened cement paste, in: Tanabe, et al., (Eds.), Proc. Creep, Shrinkage and Durability Mechanics of Concrete and Concrete Structures, 2008, pp. 49–55.
[37] C.F. Ferraris, F.H. Wittmann, Shrinkage mechanisms of hardened cement paste, Cem. Concr. Res. 17 (1987) 453–464.
[38] A.M. Neville, W.H. Dilger, J.J. Brooks, Creep of Plain and Structural Concrete, Construction Press, London, 1983.
[39] B. Bissonnette, M. Pigeon, A.M. Vaysburd, Tensile creep of concrete: study of its sensitivity to basic parameters, ACI Mater. J. 104 (4) (2007) 360–368.
[40] Z.P. Bazant, Mathematical Modeling of Creep and Shrinkage of Concrete, in: Bazant (Ed.), John Wiley & Sons Ltd., 1988
[41] Z.P. Bažant, L. Panula, Practical prediction of time-dependent deformations of concrete. Part II: basic creep, Mater. Struct. 11 (1978) 317–328.
[42] Z.P. Bažant, Input of creep and shrinkage characteristics for a structural analysis program, Mater. Struct. 15 (1982) 283–290.
[43] O. El-Mhady, T. Yamaguchi, S. Ikeda, Experimental studies on the basic creep of cement paste, Mortar and Concrete, 16(1) (1994) 615–620.
[44] Z.P. Bažant, A.A. Asghari, J. Schmidt, Experimental study of creep of hardened Portland cement paste at variable water content, Mater. Stuct. 9 (1976) 279–290.
[45] F.H. Wittmann, Einfluss des Feuchtigkeitsgehaltes auf das Kriechen des Zemensteins, Rheol. Acta 9 (1970) 282–287.
[46] Z.P. Bažant, P.C. Prat, Effect of temperature and humidity on fracture energy of concrete, ACI Mater. J. 85 (1999) 262–271.
[47] I. Carol, P. Prat, A statically constrained microplane model for smeared analysis of concrete cracking, in: Bicanic, Mang (Eds.), Computer Aided Analysis and Design of Concrete Structures, Pineridge Press, Austria, 1990, pp. 919–930.
[48] I. Carol, P. Prat, C.M. López, Normal/shear cracking model. Application to discrete crack analysis, ASCE J. Eng. Mech. 123 (1997) 765–773.
[49] A. Caballero, K.J. Willam, I. Carol, Consistent tangent formulation for 3D interface modeling of cracking/fracture in quasi-brittle materials, Comput. Meth. Appl. Mech. Eng. 197 (2008) 2804–2822.
[50] C.M. López, I. Carol, A. Aguado, Meso-structural study of concrete fracture using inter-face elements. II: compression, biaxial and Brazilian test, Mater. Struct. 41 (2008) 601–620.
[51] P.K. Mehta, P.M. Monteiro, Concrete — Microstruture, Properties and Materials, 3rd Edition McGraw-Hill, 2006.
[52] E. Stora, B. Bary, Q.-C. He, E. Deville, P. Montarnal, Modelling and simulations of the chemo-mechanical behaviour of leached cement-based materials. Leaching process and induced loss of stiffness, Cem. Concr. Res. 39 (2009) 763–772.
[53] B. Pichler, S. Scheiner, C. Hellmich, From micron-sized needle-shaped hydrates to meter-sized shotcrete tunnel shells: micromechanical upscaling of stiffness and strength of hydrating shotcrete, Acta Geotech. 3 (2008) 273–294.